CrossMark

ORIGINAL PAPER

A regularized orthotropic continuum damage model for layered composites: intralaminar damage progression and delamination

Jaan-Willem Simon[1] · Daniel Höwer[1] · Bertram Stier[2] ·
Stefanie Reese[1] · Jacob Fish[3]

Abstract Predicting progressive damage in composite materials is essential for the design of most lightweight constructions. When laminated composite structures are considered, both intralaminar and interlaminar (delamination) damage evolution need to be addressed. Typically, these different damage modes are treated separately. On the contrary, in this paper, a continuum damage model is presented which is capable of modeling orthotropic damage progression within layers as well as delamination. The model is formulated in a thermodynamically consistent manner. Moreover, the results are mesh independent due to a fracture energy based regularization scheme.

Keywords Orthotropic damage model · Thermodynamically consistent · Damage interaction · Layered composites · Delamination · Regularization

1 Introduction

In numerous engineering applications such as aerospace, automotive, and maritime industry, the use of fiber reinforced composites (FRCs) is gaining importance. Especially in lightweight constructions these materials have become very popular due to their relatively high stiffness and low weight. Modeling the mechanical behavior of such materials can be challenging because of the complexities introduced by their microstructure. In order to set up models which can be applied on the structural level (macro-scale) with an acceptable computational effort—which in most cases means with acceptable running times of the computations—and still account for effects resulting from the underlying microstructure (micro-scale), computational multiscale methods are needed. Among these, the synergistic homogenization schemes, such as the FE^2 method [30,32,33,92] or the so-called Generalized Method of cells (GMC) [2,3,14], have been used extensively. These methods rely on the handshake between the macro-scale, which is computed with the finite element method, and the micro-scale, which is called in any integration point at any step of the computation. The advantage of this approach is the fact that relatively simple material models can be used for the single constituents. On the other hand, although such methods have proven to be applicable in a broad range of applications, they can easily become computationally heavy.

Phenomenological models offer an alternative, which is much more efficient. Here, the whole composite is considered only on the structural level as one effective, homogenized material. For this, more complex material models have to be developed, which are capable of accounting for the complex anisotropic material behavior.

Predicting the damage onset and progression of composite structures is an important task. If the material is described by a phenomenological model, this can be done conveniently by using the continuum damage mechanics (CDM) approach introduced by Kachanov, see e.g. [29,41]. Recent applications of the CDM to modeling progressive damage can be found e.g. in [43,58,75] for concrete, in [57,60] for masonry, in [79] for self-healing shape polymers, [10,24,47,61,72,74]

✉ Jaan-Willem Simon
jaan.simon@rwth-aachen.de

1 Institute of Applied Mechanics, RWTH Aachen University, 52074 Aachen, Germany

2 Collier Research Corporation, HyperSizer, Newport News, VA 23606, USA

3 Department of Civil Engineering and Engineering Mechanics, Columbia University, New York, NY 10027, USA

Springer

for polymer matrix composites (PMCs), in [14,48,64] for ceramic matrix composites (CMCs), in [2] for metal matrix composites (MMCs), and in [44] for a steel wire reinforced cement beam, to name only a few.

In most applications, CDM models are formulated for the isotropic case with one single damage variable. Even so, anisotropic damage evolution can also be described within this concept by using more than one damage variables. In particular, two damage variables have been used to differentiate between tension and compression (see e.g. [19,57]), between tension and shear [84], or between the fiber and the matrix part in transversely isotropic composites [74]. Further, three damage variables can be applied to describe deviatoric, volumetric, and tangential parts [37], to differentiate between fiber (longitudinal), matrix (transverse) and shear components [46,50,81], or as the principal directions of damage progression (see e.g. [17,21,24,44,89]). In few applications, even four damage variables have been introduced describing the principal directions together with a separate hydrostatic part [2] or referring to longitudinal and two transverse directions as well as shear [51]. In the majority of anisotropic damage models, however, a general second order damage tensor is introduced. Noteworthy, almost all of the above mentioned models are or can be incorporated into this more general approach. While on the one hand it is always desirable to reduce the number of state variables to a minimum, this enforces on the other hand the formulation of the model in the principal directions of damage, which might even change during the computation. As an alternative, in the current paper, six damage variables are introduced to describe the orthotropic behavior without any coordinate transformation, see Sect. 2.1.

One well-known drawback of the CDM models is their pathological mesh dependence, which results from localization of failure, leading to an ill-posed setting of the problem (loss of ellipticity). Remedies can be achieved by introducing non-local integral operators (see e.g. [19,21,23,63]), by gradient-enhancement (see e.g. [37,56,80,85]), or by regularization schemes. The latter can be based on viscous [59] or viscoplastic [52,54,70,82] regularization, on thermal diffusion [45], or on kinematic enhancement [53]. As an alternative, the regularization can be based on the fracture energy, that is dissipated during crack opening, as introduced by Bažant and Oh [7] in the so-called crack band model. This approach has been applied frequently by several groups, e.g. [27,31,87]. Moreover, extensions to multiscale applications can be found in [43,44,60,75], whereas a probabilistic approach is proposed in [38], and an investigation of the dependence on the applied strain measure is given in [88].

Structural collapse in fiber composite structures is caused by the evolution of either intralaminar failure, such as matrix transverse cracking and fiber fracture, or interlaminar delamination. Typically, delamination is treated separately from

the intralaminar damage mechanisms. A common approach is the use of two-dimen- sional interface elements with zero thickness, the cohesive zone elements [4,18,20,36,86]. These require the definition of an appropriate criterion for the onset of delamination as well as for its growth after an initial crack has evolved. While the onset is often simply given by stress-resistance relations, see e.g. [15,26,68,73,76,90], the damage progression is described by traction-separation constitutive laws. Although cohesive zone elements are very efficient in delamination modeling, their use is restricted because of the two-dimensional formulation, which does not allow considering cohesive zones of real thickness. One attempt to overcome this restriction is using solid-shell elements instead of zero-thickness interface elements [62,67,83].

The primary goal of this manuscript is to present a phenomenological progressive damage model that possesses the following features:

1. The damage model is based on the effective stress concept and the energy equivalence hypothesis within the thermodynamically consistent framework, such that the predicted damage states are physically admissible.
2. The model enables description of anisotropic damage evolution, which is particularly important when intralaminar failure of composite materials is considered. The damage state is described by six internal variables, which can interact with each other, such that even uniaxial loading can induce damage in directions other than the loading direction.
3. Mesh dependency is cured by rescaling of the damage constitutive laws. Thereby, the dissipated energy during crack opening is guaranteed to represent the fracture energy.
4. The same model can also be used for the prediction of delamination, where different modes can be accounted for. Hence, it is suited for predicting intralaminar as well as interlaminar failure of laminated composites.

2 Consistent framework for continuum damage models

In this Section, the framework is briefly reviewed, within which the continuum damage model can be formulated in a thermodynamically consistent manner. For further details on the general framework, particularly concerning Sect. 2.2 and 2.3, the interested reader is referred to [6].

2.1 Concept of effective stress and choice of damage variables

In order to describe the damage behavior of a material, the effective stress tensor is defined by

$$\bar{\sigma}_{\alpha\beta} = M_{\alpha\beta\gamma\delta}\,\sigma_{\gamma\delta} \tag{1}$$

where Greek letters as indices run from 1 to 3. $\sigma_{\gamma\delta}$ are the components of the Cauchy stress tensor, and $\mathbb{M}$, with components $M_{\alpha\beta\gamma\delta}$, denotes the fourth order damage effect tensor. This tensor is a function of the set $\mathcal{D}$ of internal variables that characterize the damage state, $\mathbb{M} = \mathbb{M}(\mathcal{D})$.

As shown e.g. by Betten [12,13], the damage variables contained in $\mathcal{D}$ can be scalars, tensors of second order, or tensors of fourth order. In this work, six independent scalar-valued damage variables are chosen, $\mathcal{D} = \{d_1, d_2, d_3, d_4, d_5, d_6\}$. These can be interpreted as the components of either a six-dimensional damage vector $\mathbf{d} = (d_1, d_2, d_3, d_4, d_5, d_6)^T$ in Voigt-notation, a symmetric second-order damage tensor $\mathbf{D}$,

$$D_{\alpha\beta} = \begin{pmatrix} D_{11} & D_{12} & D_{13} \\ D_{21} & D_{22} & D_{23} \\ D_{31} & D_{32} & D_{33} \end{pmatrix} = \begin{pmatrix} d_1 & d_4 & d_5 \\ d_4 & d_2 & d_6 \\ d_5 & d_6 & d_3 \end{pmatrix} \tag{2}$$

or a fourth-order damage tensor $\mathbb{D}$,

$$\mathbb{D} = \sum_{\alpha=1}^{3}\sum_{\beta=1}^{3} \frac{1}{2} D_{\alpha\beta} \left(\mathbf{e}_\alpha \otimes \mathbf{e}_\beta \otimes \mathbf{e}_\alpha \otimes \mathbf{e}_\beta \right.$$
$$\left. + \mathbf{e}_\alpha \otimes \mathbf{e}_\beta \otimes \mathbf{e}_\beta \otimes \mathbf{e}_\alpha \right) \tag{3}$$

For the following derivations, it is useful to express $\mathbb{D}$ also in terms of the contracted six-by-six matrix $\hat{\mathbb{D}}$ in Voigt-notation,

$$\hat{D}_{ij} = \begin{bmatrix} D_{11} & 0 & 0 & 0 & 0 & 0 \\ 0 & D_{22} & 0 & 0 & 0 & 0 \\ 0 & 0 & D_{33} & 0 & 0 & 0 \\ 0 & 0 & 0 & D_{12} & 0 & 0 \\ 0 & 0 & 0 & 0 & D_{13} & 0 \\ 0 & 0 & 0 & 0 & 0 & D_{23} \end{bmatrix} \tag{4}$$

2.2 Complementary energy equivalence hypothesis

The concept of effective stress can only be applied reasonably, if additionally a damage equivalence hypothesis is made. There are two possible choices: the strain equivalence hypothesis, which has been used extensively by e.g. Lemaitre and Chaboche [16,39–41], and the complementary energy equivalence hypothesis suggested by Sidoroff [65]. In the current work, the complementary energy equivalence hypothesis is applied, which states that the complementary energy χ remains unchanged if damage occurs:

$$\chi = \chi(\boldsymbol{\sigma}, \mathcal{D}) = \chi(\bar{\boldsymbol{\sigma}}, \mathbf{0}) \tag{5}$$

The complementary energy links the engineering strain tensor $\boldsymbol{\varepsilon}$ to the Cauchy stress tensor $\boldsymbol{\sigma}$ by

$$\varepsilon_{\alpha\beta}(\boldsymbol{\sigma}, \mathcal{D}) = \frac{\partial \chi(\boldsymbol{\sigma}, \mathcal{D})}{\partial \sigma_{\alpha\beta}} \tag{6}$$

Further, the effective compliance tensor $\bar{\mathbb{S}}$, with components $\bar{S}_{\alpha\beta\gamma\delta}$, also relates $\boldsymbol{\varepsilon}$ to $\boldsymbol{\sigma}$ by

$$\varepsilon_{\alpha\beta} = \bar{S}_{\alpha\beta\gamma\delta}\,\sigma_{\gamma\delta} \tag{7}$$

and thus can be expressed through the complementary energy,

$$\bar{S}_{\alpha\beta\gamma\delta} = \frac{\partial^2 \chi(\boldsymbol{\sigma}, \mathcal{D})}{\partial \sigma_{\alpha\beta}\,\sigma_{\gamma\delta}} \tag{8}$$

As shown e.g. in [25,91], this yields to the following relation between the effective compliance tensor $\bar{\mathbb{S}}$ and the undamaged one $\mathbb{S}$:

$$\bar{S}_{\alpha\beta\gamma\delta} = M_{\epsilon\rho\alpha\beta}\,S_{\epsilon\rho\eta\theta}\,M_{\eta\theta\gamma\delta} \tag{9}$$

Again, it is useful to express this relation also in terms of the contracted six-by-six matrices $\hat{\bar{\mathbb{S}}}$, $\hat{\mathbb{M}}$ and $\hat{\mathbb{S}}$ in Voigt-notation,

$$\hat{\bar{S}}_{ij} = \hat{M}_{ki}\,\hat{S}_{kl}\,\hat{M}_{lj} \tag{10}$$

where Latin letters as indices run from 1 to 6.

2.3 Thermodynamically consistent description of damage onset and propagation

In this Subsection, the description of damage onset and damage propagation are given, which lead to a thermodynamically consistent formulation, see e.g. Krajcinovic [34,35]. All tensors are expressed in Voigt-notation, and hence the $(\hat{.})$ is omitted in the following in order to simplify notations.

Starting point is the complementary energy $\chi(\boldsymbol{\sigma}, \boldsymbol{d})$. The thermodynamic driving forces $\boldsymbol{Y}(\boldsymbol{\sigma}, \boldsymbol{d})$—representing the thermodynamically conjugated quantities to the damage variables — can then be obtained from

$$Y_i(\boldsymbol{\sigma}, \boldsymbol{d}) = \rho\,\frac{\partial \chi(\boldsymbol{\sigma}, \boldsymbol{d})}{\partial d_i}, \tag{11}$$

where ρ denotes the mass density. In order to define the damage onset as well as the hardening or softening behavior, respectively, the damage surface is defined as

$$f(\boldsymbol{Y}(\boldsymbol{d}), \delta) = \hat{f}(\boldsymbol{Y}(\boldsymbol{d})) - \gamma(\delta) \tag{12}$$

Here, $\hat{f}$ can be interpreted as an equivalent thermodynamic driving force, while $\gamma(\delta)$ is the hardening/softening function expressed through the hardening/softening variable δ.

Within the associative concept used here, the evolution of damage and hardening/softening variables, respectively, are given by

$$\dot{d}_i = \dot{\lambda} \frac{\partial f}{\partial Y_i} \qquad \dot{\delta} = \dot{\lambda} \frac{\partial f}{\partial \gamma} \tag{13}$$

where the magnitude of the damage rate is represented by the damage multiplier $\dot{\lambda}$.

Whenever the stress is high enough to generate a thermodynamic driving force which yields $f = 0$, damage is accumulating. On the contrary, if $f < 0$, for example in the case of unloading, damage does not evolve. Moreover, healing effects are not considered, such that damage can only grow, $\dot{\lambda} \geq 0$. These conditions can be summarized through the Kuhn–Tucker-conditions:

$$\dot{\lambda} \geq 0 \qquad f \leq 0 \qquad \dot{\lambda} f = 0 \tag{14}$$

2.4 Computing the damage multiplier

To compute the damage multiplier $\dot{\lambda}$, the consistency condition is utilized, which reads

$$\dot{f} = \frac{\partial f}{\partial Y_k} \dot{Y}_k + \frac{\partial f}{\partial \delta} \dot{\delta} = 0 \tag{15}$$

Substituting the rate of the thermodynamic driving forces

$$\dot{Y}_i = \frac{\partial Y_i}{\partial \sigma_k} \dot{\sigma}_k + \frac{\partial Y_i}{\partial d_l} \dot{d}_l \tag{16}$$

into (15) and making use of the evolution equations (13) yields the following expression

$$\dot{\lambda} = - \frac{\dfrac{\partial f}{\partial Y_k} \dfrac{\partial Y_k}{\partial \sigma_l} \dot{\sigma}_l}{\dfrac{\partial f}{\partial Y_m} \dfrac{\partial Y_m}{\partial d_n} \dfrac{\partial f}{\partial Y_n} + \dfrac{\partial f}{\partial \delta} \dfrac{\partial f}{\partial \gamma}} \tag{17}$$

An elastic predictor–damage corrector return mapping algorithm is used to solve for the variables. For this, following [5] and [78], the time discretization between two consecutive iterations $K - 1$ and K is applied for the consistency condition (15),

$$f^K - f^{K-1} \cong \left. \left(\frac{\partial f}{\partial Y_m} \frac{\partial Y_m}{\partial d_n} \right) \right|^{K-1} \left(d_n^K - d_n^{K-1} \right)$$
$$+ \left. \frac{\partial f}{\partial \delta} \right|^{K-1} \left(\delta^K - \delta^{K-1} \right) = 0 \tag{18}$$

as well as for the evolution equations (13),

$$d_i^K - d_i^{K-1} \cong \Delta \lambda^K \left. \frac{\partial f}{\partial Y_i} \right|^{K-1} \tag{19}$$

$$\delta^K - \delta^{K-1} \cong \Delta \lambda^K \left. \frac{\partial f}{\partial \gamma} \right|^{K-1} \tag{20}$$

Thereby, the first-order linearization of the consistency condition reads

$$f^K - f^{K-1} \cong \Delta \lambda^K \left. \left(\frac{\partial f}{\partial Y_m} \frac{\partial Y_m}{\partial d_n} \frac{\partial f}{\partial Y_n} + \frac{\partial f}{\partial \delta} \frac{\partial f}{\partial \gamma} \right) \right|^{K-1} \tag{21}$$

Since successful iterations yield $f^K = 0$, the damage multiplier is thus computed from

$$\Delta \lambda^K = - \frac{f^{K-1}}{\left. \left(\dfrac{\partial f}{\partial Y_m} \dfrac{\partial Y_m}{\partial d_n} \dfrac{\partial f}{\partial Y_n} + \dfrac{\partial f}{\partial \delta} \dfrac{\partial f}{\partial \gamma} \right) \right|^{K-1}} \tag{22}$$

3 Specific choice of model functions

In order to complete the model equations, specific choices for the complementary energy function χ and for the damage surface f have to be made. In the current work, an extension of the two-dimensional model suggested by Barbero (2013) [6] to the 3D-case has been applied, as proposed recently by the authors [11].

3.1 Chosen form of the Complementary Energy

To define an orthotropic model, the following quadratic form is chosen for the complementary energy:

$$\chi(\boldsymbol{\sigma}, \boldsymbol{d}) = \frac{1}{2\rho} \sigma_i \bar{S}_{ij} \sigma_j = \frac{1}{2\rho} \bar{\sigma}_k S_{kl} \bar{\sigma}_l =$$
$$\frac{1}{2\rho} \left[\frac{\sigma_1^2}{(1-d_1)^2 E_1} + \frac{\sigma_2^2}{(1-d_2)^2 E_2} + \frac{\sigma_3^2}{(1-d_3)^2 E_3} \right.$$
$$+ \frac{\sigma_4^2}{(1-d_4)^2 G_{12}} + \frac{\sigma_5^2}{(1-d_5)^2 G_{13}} + \frac{\sigma_6^2}{(1-d_6)^2 G_{23}}$$
$$- \alpha_{12} \frac{\sigma_1 \sigma_2}{(1-d_1)(1-d_2)} - \alpha_{13} \frac{\sigma_1 \sigma_3}{(1-d_1)(1-d_3)}$$
$$\left. - \alpha_{23} \frac{\sigma_2 \sigma_3}{(1-d_2)(1-d_3)} \right] \tag{23}$$

where

$$\alpha_{12} = \frac{\nu_{12}}{E_1} + \frac{\nu_{21}}{E_2} \qquad \alpha_{13} = \frac{\nu_{13}}{E_1} + \frac{\nu_{31}}{E_3} \qquad \alpha_{23} = \frac{\nu_{23}}{E_2} + \frac{\nu_{32}}{E_3} \tag{24}$$

and E_1, E_2, E_3, G_{12}, G_{13}, G_{23}, ν_{12}, ν_{13}, and ν_{23} are the pristine (undamaged) Young's moduli, shear moduli, and Poisson's ratios, respectively. Then, the thermodynamic driving forces defined in (11) can be written as

$$Y_1 = \frac{\sigma_1^2}{E_1(1-d_1)^3} - \frac{\nu_{12}}{E_1}\frac{\sigma_1\,\sigma_2}{(1-d_1)^2(1-d_2)}$$
$$- \frac{\nu_{13}}{E_1}\frac{\sigma_1\,\sigma_3}{(1-d_1)^2(1-d_3)} \tag{25a}$$

$$Y_2 = \frac{\sigma_2^2}{E_2(1-d_2)^3} - \frac{\nu_{21}}{E_2}\frac{\sigma_1\,\sigma_2}{(1-d_1)(1-d_2)^2}$$
$$- \frac{\nu_{23}}{E_2}\frac{\sigma_2\,\sigma_2}{(1-d_2)^2(1-d_3)} \tag{25b}$$

$$Y_3 = \frac{\sigma_3^2}{E_3(1-d_3)^3} - \frac{\nu_{31}}{E_3}\frac{\sigma_1\,\sigma_3}{(1-d_1)(1-d_3)^2}$$
$$- \frac{\nu_{32}}{E_3}\frac{\sigma_2\,\sigma_3}{(1-d_2)(1-d_3)^2} \tag{25c}$$

$$Y_4 = \frac{\sigma_4^2}{G_{12}(1-d_4)^3} \tag{25d}$$

$$Y_5 = \frac{\sigma_5^2}{G_{13}(1-d_5)^3} \tag{25e}$$

$$Y_6 = \frac{\sigma_6^2}{G_{23}(1-d_6)^3} \tag{25f}$$

Furthermore, the effective compliance tensor defined in (8) reads

$$\bar{S}_{ij} = \begin{bmatrix} \bar{S}_{11} & \bar{S}_{12} & \bar{S}_{13} & 0 & 0 & 0 \\ \bar{S}_{21} & \bar{S}_{22} & \bar{S}_{23} & 0 & 0 & 0 \\ \bar{S}_{31} & \bar{S}_{32} & \bar{S}_{33} & 0 & 0 & 0 \\ 0 & 0 & 0 & \bar{S}_{44} & 0 & 0 \\ 0 & 0 & 0 & 0 & \bar{S}_{55} & 0 \\ 0 & 0 & 0 & 0 & 0 & \bar{S}_{66} \end{bmatrix} \tag{26}$$

where

$$\bar{S}_{11} = \frac{1}{E_1(1-d_1)^2} \qquad \bar{S}_{22} = \frac{1}{E_2(1-d_2)^2} \tag{27}$$

$$\bar{S}_{33} = \frac{1}{E_3(1-d_3)^2} \qquad \bar{S}_{44} = \frac{1}{G_{12}(1-d_4)^2} \tag{28}$$

$$\bar{S}_{55} = \frac{1}{G_{13}(1-d_5)^2} \qquad \bar{S}_{66} = \frac{1}{G_{23}(1-d_6)^2} \tag{29}$$

and

$$\bar{S}_{12} = -\frac{\nu_{12}}{E_1(1-d_1)(1-d_2)} \tag{30}$$

$$= -\frac{\nu_{21}}{E_2(1-d_1)(1-d_2)} = \bar{S}_{21} \tag{31}$$

$$\bar{S}_{13} = -\frac{\nu_{13}}{E_1(1-d_1)(1-d_3)} \tag{32}$$

$$= -\frac{\nu_{31}}{E_3(1-d_1)(1-d_3)} = \bar{S}_{31} \tag{33}$$

$$\bar{S}_{23} = -\frac{\nu_{23}}{E_2(1-d_2)(1-d_3)} \tag{34}$$

$$= -\frac{\nu_{32}}{E_3(1-d_2)(1-d_3)} = \bar{S}_{32} \tag{35}$$

From (26) and (10) it is obvious, that with the definition of χ a choice for the damage effect tensor introduced in (1) is also made implicitly, such that

$$M_{mn} = \frac{1}{(1-d_m)}\,\delta_{mn} \quad \text{(no summation over } m) \tag{36}$$

which is the contraction of the fourth-order tensor

$$\mathbb{M} = (\mathbb{I} - \mathbb{D})^{-1} \tag{37}$$

where $\mathbb{I}$ is the fourth-order identity tensor, and $\mathbb{D}$ is the fourth-order damage tensor defined in (3). Finally, the effective stress is thus simply given by

$$\bar{\sigma}_n = \frac{\sigma_n}{(1-d_n)} \quad \text{(no summation over } n) \tag{38}$$

It is worth to mention, that in most applications this damage effect tensor is defined in terms of the three principal values of damage (see e.g. [17,21,24,44,89]). Then, the 44-, 55-, and 66-components depend also on these three damage variables. Nevertheless, following the approach presented in e.g. [46] (for 2D), independent damage variables are used here to allow for higher flexibility. The interested reader is also referred to [81].

3.2 Chosen form of the damage surface

In order to describe the damage surface $f = \hat{f} - \gamma$, the two functions $\hat{f}(Y)$ and $\gamma(\delta)$ are defined as follows:

$$\hat{f}(Y) = (Y_k\,H_{kl}\,Y_l)^{1/2} \tag{39}$$
$$\gamma(\delta) = c_1(e^{\delta/c_2} - 1) + \gamma_0 \tag{40}$$

where $H_{ij} \geq 0$ are material parameters responsible for the interaction of the damage variables' effect on the stiffness reduction of the material. Noteworthy, this expression for $\hat{f}(Y)$ can also be interpreted as the second invariant Y_{II} of the damage strain energy release rate Y proposed in [17]. Further, $\gamma_0 > 0$ is the initial damage threshold, and $c_1 > 0$ as well as $c_2 < 0$ are model parameters.

It is worth to mention, that this choice leads to a damage threshold γ with the dimension of a critical energy release rate, which is always increasing irrespective of whether hardening or softening occur. Therefore, the hardening/softening variable δ is always negative and decreasing. On the contrary, had a stress threshold been used instead, it would be either increasing (hardening) or decreasing (softening).

The derivatives of the damage surface read

$$\frac{\partial f}{\partial Y_i} = \frac{\partial \hat{f}}{\partial Y_i} = \frac{H_{ij} Y_j}{(Y_k H_{kl} Y_l)^{1/2}} \tag{41}$$

$$\frac{\partial f}{\partial \gamma} = -1 \tag{42}$$

$$\frac{\partial f}{\partial \delta} = -\frac{\partial \gamma}{\partial \delta} = -\frac{c_1}{c_2} e^{\delta/c_2} \tag{43}$$

Substituting these derivatives into (13) the evolution equations can be expressed as

$$\dot{d}_i = \dot{\lambda} \frac{\partial f}{\partial Y_i} = \dot{\lambda} \frac{H_{ij} Y_j}{(Y_k H_{kl} Y_l)^{1/2}} \qquad \dot{\delta} = \dot{\lambda} \frac{\partial f}{\partial \gamma} = -\dot{\lambda} \tag{44}$$

Analogously, substitution of (43) into (22) yields the damage multiplier

$$\Delta\lambda^K = -\frac{f^{K-1}}{\left(\frac{H_{mp} Y_p H_{nq} Y_q}{Y_k H_{kl} Y_l} \frac{\partial Y_m}{\partial d_n} + \frac{c_1}{c_2} e^{\delta/c_2}\right)\Big|^{K-1}} \tag{45}$$

where the derivative $\partial Y_m/\partial d_n$ can be obtained from (25).

4 Variety of describable damage effects

The proposed model can be used in a broad spectrum of applications. One reason for that is the chosen form of the hardening/softening function $\gamma(\delta)$ in Eq. (40), which is indeed able to describe both hardening and softening behavior. In addition, by choosing the damage interaction parameters H_{ij} appropriately, several different damage scenarios can be accounted for as will be shown below.

4.1 Fitting the hardening/softening function

The material parameters c_1, c_2, and γ_0 can be fitted easily to the result of an uniaxial tension test. For example, assume that the stress–strain data in 3-direction have been obtained from a tensile test, in which the boundary conditions have been applied such that the stress state has been approximately uniaxial and homogeneous. Then, only one component Y_3 of the thermodynamic driving forces is non-zero. In this case, the damage surface defined by (39) and (40) reads:

$$f = \sqrt{H_{33}} Y_3 - \left(c_1(e^{\delta/c_2} - 1) + \gamma_0\right) = 0 \tag{46}$$

If damage onset is considered, no damage has occurred yet, $d_i = 0$ and $\delta = 0$, leading to

$$\gamma_0 = \sqrt{H_{33}} Y_3 = \sqrt{H_{33}} \frac{(\sigma_3^0)^2}{E_3} = \sqrt{H_{33}} (\varepsilon_3^0)^2 E_3 \tag{47}$$

where σ_3^0 and ε_3^0 denote the stress and the strain in 3-direction at damage onset, respectively. Noteworthy, the first value of the damage interaction parameters H_{ij} can be chosen arbitrarily. To show this, assume that $\bar{c}_1$, $\bar{c}_2$, and $\bar{\gamma}_0$ have been determined already using a particular value $\bar{H}_{33}$. Then, the exact same damage surface and evolution equations can be obtained by replacing these parameters by

$$H_{33}^* = 1 \quad c_1^* = \frac{\bar{c}_1}{\sqrt{\bar{H}_{33}}} \quad c_2^* = \sqrt{\bar{H}_{33}}\, \bar{c}_2 \quad \gamma_0^* = \frac{\bar{\gamma}_0}{\sqrt{\bar{H}_{33}}} \tag{48}$$

Hence, the first parameter can be chosen arbitrarily, e.g. $H_{33} = 1$, and for the interactions of damage only the ratios of these parameters are relevant. Then, the damage threshold is obtained as

$$\gamma_0 = \frac{(\sigma_3^0)^2}{E_3} = (\varepsilon_3^0)^2 E_3 \tag{49}$$

Next, the two parameters c_1 and c_2 are to be determined. For this, two points $(\sigma_3^I, \varepsilon_3^I)$ and $(\sigma_3^{II}, \varepsilon_3^{II})$ have to be chosen from the part of the curve in which damage has already occurred. These points should not be too close to each other. For these values, using the relation $\sigma_3 = (1 - d_3)^2 E_3 \varepsilon_3$, the damage variables are computed from

$$d_3^I = 1 - \sqrt{\frac{\sigma_3^I}{E_3 \varepsilon_3^I}} \qquad d_3^{II} = 1 - \sqrt{\frac{\sigma_3^{II}}{E_3 \varepsilon_3^{II}}} \tag{50}$$

Having these damage variables d_3^I and d_3^{II}, the following equation, whose derivation can be found in the Appendix, can be solved directly for c_2:

$$a_2 (e^{-d_3^I/c_2} - 1) - a_1 (e^{-d_3^{II}/c_2} - 1) = 0 \tag{51}$$

$$\text{where:} \quad a_1 = (1 - d_3^I)E_3(\varepsilon_3^I)^2 - \gamma_0 \tag{52}$$

$$a_2 = (1 - d_3^{II})E_3(\varepsilon_3^{II})^2 - \gamma_0 \tag{53}$$

Finally, the remaining parameter is obtained from

$$c_1 = \frac{a_1}{(e^{-d_3^I/c_2} - 1)} \tag{54}$$

In some cases, the full stress–strain data is not available but only one point $(\sigma_3^I, \varepsilon_3^I)$ of the curve, e.g. the peak values, and the corresponding fracture energy in tension (mode I) G_{Ic}. Then, the parameters have to be determined from an iterative procedure. First, the damage variable d_3^I is calculated as in (50) above. Then, a value for c_2 is guessed reasonably. Thereby, the parameter c_1 is also set according to (54). With these parameters, the stress–strain response can be computed. In Fig. 1, the stress–strain plots for several different choices of c_2 are shown, all generated through the
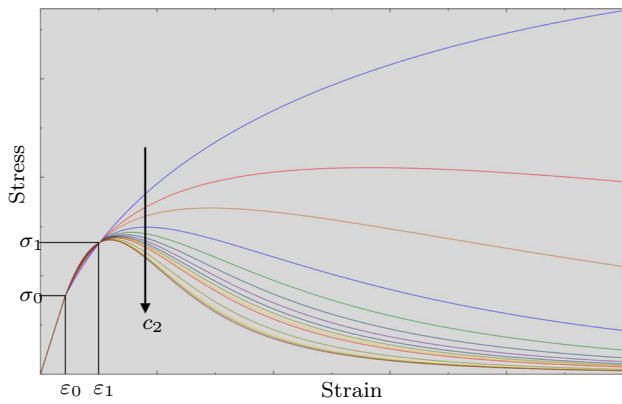
Fig. 1 Variation of parameter c_2 with constant γ_0 and c_1 according to (54)

same point $(\sigma_1, \varepsilon_1)$. As one can see, the function allows for a broad variety of material response in hardening as well as softening.

In order to fix the parameters, the dissipated energy G_I is evaluated based on the area under the stress–strain curve (see Sect. 5 for more details). If this G_I is larger than the fracture energy G_{Ic}, then the parameter c_2 has been chosen too large and should be decreased. The closer the computed energy is to the fracture energy, $G_I \approx G_{Ic}$, the better is the fit of the two parameters c_1 and c_2.

4.2 Special choices for the damage interaction parameters

The parameters H_{ij} represent the interaction of the damage variables. To show the effect of these parameters, consider for example a loading in 3-direction, $Y_3 \neq 0$, while all other components of Y_i are zero. Then, the evolution equation (44) for the damage variables reads

$$\dot{d}_i = \dot{\lambda} \frac{H_{ij} Y_j}{(Y_k H_{kl} Y_l)^{1/2}} = \dot{\lambda} \frac{H_{i3} Y_3}{(Y_3 H_{33} Y_3)^{1/2}} = \dot{\lambda} \frac{H_{i3}}{\sqrt{H_{33}}} \quad (55)$$

From this relation the role of the damage interaction parameters becomes obvious. For example, the damage evolution in 2-direction $\dot{d}_2$ due to the loading in 3-direction is described by the parameter $H_{23} = H_{32}$. In fact, as already mentioned above, only the ratio between H_{23} and $\sqrt{H_{33}}$ plays a role.

For the determination of these parameters from experiments, biaxial tests have to be performed. For example can the parameter H_{14} be obtained from a tension-torsion experiment, whereas for H_{23} a biaxial tension test (tensile loading in 2-direction and 3-direction independently of each other) is needed.

By choosing the interaction parameters H_{ij} appropriately, different material behavior can be described by the presented model, as is shown below.

4.2.1 Isotropic damage model with full interaction

The isotropic damage model with only one damage variable d is probably the most used one in literature. This model is obtained by utilizing the following interaction parameters:

$$H_{ij} = H \begin{bmatrix} 1 & 1 & 1 & 1 & 1 & 1 \\ 1 & 1 & 1 & 1 & 1 & 1 \\ 1 & 1 & 1 & 1 & 1 & 1 \\ 1 & 1 & 1 & 1 & 1 & 1 \\ 1 & 1 & 1 & 1 & 1 & 1 \\ 1 & 1 & 1 & 1 & 1 & 1 \end{bmatrix} \quad (56)$$

The arbitrary parameter H can be omitted here. Then, the damage variables are the same in all directions,

$$\dot{d} := \dot{d}_1 = \dot{d}_2 = \dot{d}_3 = \dot{d}_4 = \dot{d}_5 = \dot{d}_6 = \dot{\lambda} \frac{\sum_{i=1}^{6} Y_i}{\sqrt{Y_k Y_k}} \quad (57)$$

The effective stress and the effective compliance are given by the following well-known expressions:

$$\bar{\sigma}_i = \frac{\sigma_i}{(1-d)} \qquad \bar{S}_{ij} = \frac{S_{ij}}{(1-d)^2} \quad (58)$$

This model can be applied to describe the evolution of damage induced by the growth of spherical micro-voids. Even if the applied loading is acting only in one particular direction, the material is isotropically damaged in all directions.

4.2.2 Damage model without interaction

If one assumes, that the damage evolution in different directions is completely independent of each other, then the corresponding interaction parameters are

$$H_{ij} = \begin{bmatrix} H_{11} & 0 & 0 & 0 & 0 & 0 \\ 0 & H_{22} & 0 & 0 & 0 & 0 \\ 0 & 0 & H_{33} & 0 & 0 & 0 \\ 0 & 0 & 0 & H_{44} & 0 & 0 \\ 0 & 0 & 0 & 0 & H_{55} & 0 \\ 0 & 0 & 0 & 0 & 0 & H_{66} \end{bmatrix} \quad (59)$$

In this case, the rates of the damage variables are

$$\dot{d}_i = \dot{\lambda} \frac{H_{ii} Y_i}{\sqrt{\sum_{k=1}^{6} H_{kk} Y_k^2}} \quad \text{(no summation)} \quad (60)$$

Obviously, damage can only occur in directions of loading. No matter how large the applied loading is, it can never effect any other direction than the loading direction. It is worth to mention, that even if the parameters are chosen to be equal, $H := H_{11} = H_{22} = H_{33} = H_{44} = H_{55} = H_{66}$, this model is different from the isotropic one described in Sect. 4.2.1. Even in this special case the damage variables evolve differently if different loads are applied.

4.2.3 Damage model for penny-shaped micro-cracks

One common assumption for damage induced by so-called penny-shaped micro-cracks is that only some very particular damage mechanisms interact with each other. For example, if the load $Y_3 \neq 0$ is applied such that damage occurs, then only the corresponding normal component in 3-direction and the shear components in 13-direction and 23-direction, respectively, are effected. Hence, in pure normal loading the damage variables are completely uncoupled. The damage interaction parameters are

$$H_{ij} = \begin{bmatrix} H_{11} & 0 & 0 & H_{14} & H_{15} & 0 \\ 0 & H_{22} & 0 & H_{24} & 0 & H_{26} \\ 0 & 0 & H_{33} & 0 & H_{35} & H_{36} \\ H_{14} & H_{24} & 0 & H_{44} & H_{45} & H_{46} \\ H_{15} & 0 & H_{35} & H_{45} & H_{55} & H_{56} \\ 0 & H_{26} & H_{36} & H_{46} & H_{56} & H_{66} \end{bmatrix} \tag{61}$$

Moreover, in most applications a decoupling of the shear components is assumed as well, $H_{45} = H_{46} = H_{56} = 0$. If additionally isotropic behavior is considered, only three different damage interaction parameters are remaining:

$$H_n := H_{11} = H_{22} = H_{33} \tag{62}$$
$$H_{ns} := H_{14} = H_{15} = H_{24} = H_{26} = H_{35} = H_{36} \tag{63}$$
$$H_s := H_{44} = H_{55} = H_{66} \tag{64}$$

leading to

$$H_{ij} = \begin{bmatrix} H_n & 0 & 0 & H_{ns} & H_{ns} & 0 \\ 0 & H_n & 0 & H_{ns} & 0 & H_{ns} \\ 0 & 0 & H_n & 0 & H_{ns} & H_{ns} \\ H_{ns} & H_{ns} & 0 & H_s & 0 & 0 \\ H_{ns} & 0 & H_{ns} & 0 & H_s & 0 \\ 0 & H_{ns} & H_{ns} & 0 & 0 & H_s \end{bmatrix} \tag{65}$$

4.2.4 Damage model for delamination

Delamination of layers in laminated structures can be considered as one special case of damage induced by penny-shaped micro-cracks. When delamination between two layers is taken into account, then only the three stress components
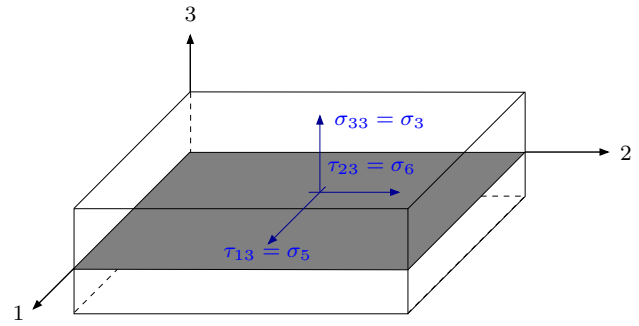
Fig. 2 Stress components within the interface between two layers which have an effect on delamination

acting at the interface have an effect on the onset and progression of damage. If, for example, an interface with the 3-direction as normal direction is considered, the only the stress components $\sigma_{33} = \sigma_3$, $\tau_{13} = \sigma_5$, and $\tau_{23} = \sigma_6$ can lead to delamination, see Fig. 2.

Consequently, for delamination in a plane with the 3-direction as normal direction, the damage interaction parameters are given as

$$H_{ij} = \begin{bmatrix} 0 & 0 & 0 & 0 & 0 & 0 \\ 0 & 0 & 0 & 0 & 0 & 0 \\ 0 & 0 & H_n & 0 & H_{ns} & H_{ns} \\ 0 & 0 & 0 & 0 & 0 & 0 \\ 0 & 0 & H_{ns} & 0 & H_s & H_{ss} \\ 0 & 0 & H_{ns} & 0 & H_{ss} & H_s \end{bmatrix} \tag{66}$$

where for most materials it is reasonable to assume that a shear loading σ_5 induces the same damage in terms of stiffness reduction in 5- and 6-direction, i.e. $H_s = H_{ss}$. Then, only two independent damage variables d_n and d_s exist, whose evolution equations read

$$\dot{d}_n = \dot{d}_3 = \dot{\lambda} \frac{H_n Y_3 + H_{ns}(Y_5 + Y_6)}{\hat{f}(Y_3, Y_5, Y_6)} \tag{67}$$

$$\dot{d}_s = \dot{d}_5 = \dot{d}_6 = \dot{\lambda} \frac{H_{ns} Y_3 + H_s(Y_5 + Y_6)}{\hat{f}(Y_3, Y_5, Y_6)} \tag{68}$$

where

$$\hat{f}(Y_3, Y_5, Y_6) = \sqrt{H_n Y_3^2 + 2H_{ns} Y_3(Y_5 + Y_6) + H_s(Y_5 + Y_6)^2} \tag{69}$$

The remaining damage variables are zero.

5 Regularization through rescaling of the constitutive law

Progressive continuum damage models generally suffer from a pathological mesh dependence as long as they are formulated locally. There are several approaches to cure this mesh dependence, most of them relying either on non-local theories or rescaling of damage mechanics constitutive laws. For both methodologies, the interested reader is referred to the book of Bažant and Planas [9]. As shown recently by Liu et al. [44], these formulations yield the same results provided that they are driven by the same quantity—the effective softening strain κ_s. Therefore, in the current work, the effective strain κ is decomposed into an effective softening strain κ_s related to the softening branch and an effective hardening strain κ_h, $\kappa = \kappa_s + \kappa_h$. Then, rescaling of the constitutive laws is performed based on the softening strain only. Furthermore, the softening strain can be defined according to Bažant and Pijaudier-Cabot [8] as shown schematically in Fig. 3 for the unidirectional case. The softening strain is therefore given by

$$\kappa_s = \kappa - \kappa_h = \kappa - \frac{\sigma}{\sigma_p}\kappa_p \qquad (70)$$

where σ_p and κ_p are the peak values of the stress-softening strain curve.

The dissipated energy per unit volume g_s is then defined as the area under the stress-softening strain curve (see Fig. 3). This value represents the energy, which is dissipated from the system due to the deletion of the considered element e, divided by its characteristic element length $h_e := \Omega_e/S_e$, where Ω_e and S_e denote the element volume and the created free surface, respectively. For regular tetrahedral elements, the element height can be used as characteristic element length if the element is aligned in direction of the crack band. However, in more complex situations, more sophisticated strategies should be applied as shown in [28,55].
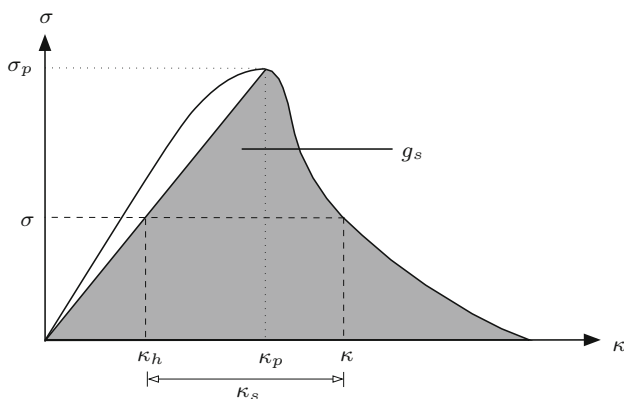
Fig. 3 Definition of the softening strain κ_s
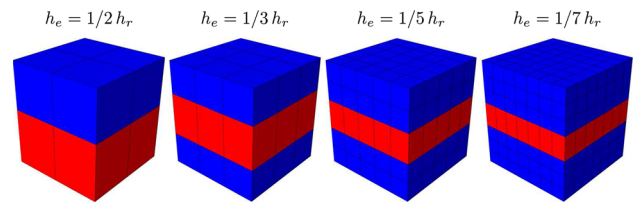
Fig. 4 Simple tension block test with different discretizations: $2^3 = 8$ elements, $3^3 = 27$ elements, $5^3 = 125$ elements, $7^3 = 343$ elements; *blue*: undamaged; *red*: damaged. (Color figure online)

Noteworthy, even if the element is not actually deleted during the computation, g_s still represents the dissipated energy at complete failure, since the element does effectively no longer exist once the stress has decreased to zero. Therefore, denoting the fracture energy (toughness) by G_c, it is clear that $G_c = g_s h_e$ has to hold for any element size h_e. Since G_c is a material constant, the mesh dependence can be cured by rescaling the constitutive damage laws to the ratio h_e/h_r, where h_r is the element length of a reference mesh, which has been used for calibration of the material model. That is, the constitutive damage laws have to be rescaled such that for the new h_e the same dissipated energy is obtained. Hence, the parameters have to be redetermined for any new element size, such that $g_s = G_c/h_e$.

To illustrate the rescaling strategy, a simple tension block test is performed with different discretizations (see Fig. 4), which has been inspired by [22]. The material is assumed to be isotropic. The block size is held constant, such that the different discretizations lead to different element sizes. The block is fixed in vertical direction at the bottom, whereas at the top a tensile loading is applied by prescribing the displacement in vertical direction. The model parameters c_1 and c_2 have been fitted initially to the reference mesh with $h_r = 1$, which corresponds to the mesh with only one element.

If the different meshes are computed without rescaling, then the resulting force-displacement curves differ significantly, as shown in Fig. 5(a). Only by rescaling the material model, i.e. by changing the model parameters c_1 and c_2 such that the dissipated energy remains constant, the result becomes mesh-independent, as can be seen in Fig. 5(b).

It should be mentioned that the proposed regularization scheme does not guarantee to remedy potential directional mesh bias. In the computations performed in the current work, no influence of mesh orientation was observed. Nevertheless, for future studies the extension proposed by Slobbe et al. [69] will be adopted.

6 Numerical results

The proposed model has been implemented into an user-defined material constitutive subroutine (UMAT) in Abaqus
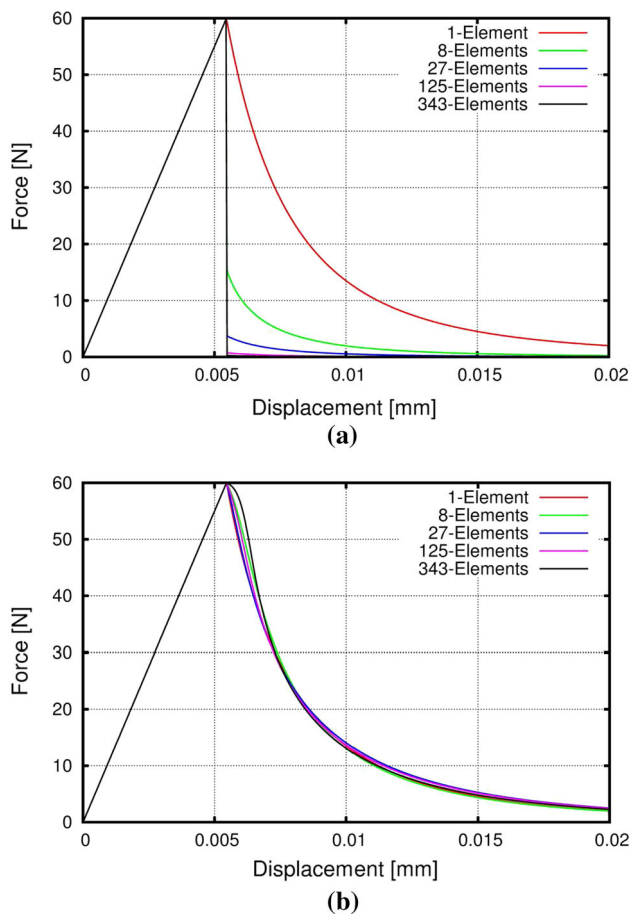
Fig. 5 Force-displacement response of simple tension block test with different discretizations. **a** Without regularization; **b** with regularization

[1]. When applied to composite laminates, it is capable of treating both, the intralaminar damage progression within each layer and the interlaminar damage mechanisms between layers (delamination).

When intralaminar damage is to be investigated, it is important to distinguish between layers made from composites with unidirectional fibers and those with textile reinforcement. Thus, to illustrate the modeling capabilities of intralaminar damage progression, two examples are presented in the following: one with unidirectional fibers taken from [72] and another one with textile reinforcement taken from [11], respectively.

Thereafter, new results for the prediction of delamination in layered composite structures are presented, which can also be obtained using the proposed damage model.

6.1 Damage analysis of unidirectional fiber reinforced composites at the micro-scale

The first example was the damage analysis of the microstructure of an unidirectional fiber reinforced composite. A sample

with 15 fibers with random locations was considered, and periodic boundary conditions were applied by using equation constraints for the degrees of freedom on opposite corners, edges, and faces of the considered volume element. The sample was meshed with 13,202 solid elements C3D8. The considered micro-structure was loaded displacement-driven by transverse tension in horizontal direction.

The fibers were made from carbon, whereas the matrix material was an epoxy resin. Hence, the fibers were assumed transversely isotropic and linear elastic, while for the matrix material the damage model without interaction of the damage variables was applied, see Sect. 4.2.2. The damage interaction parameters were

$$
H_{ij} = \begin{bmatrix}
H_n & 0 & 0 & 0 & 0 & 0 \\
0 & H_n & 0 & 0 & 0 & 0 \\
0 & 0 & H_n & 0 & 0 & 0 \\
0 & 0 & 0 & H_s & 0 & 0 \\
0 & 0 & 0 & 0 & H_s & 0 \\
0 & 0 & 0 & 0 & 0 & H_s
\end{bmatrix}
\tag{71}
$$

which represented the special case of (59) for isotropic behavior in normal and shear directions, respectively. The model parameters γ_0, c_1, and c_2 as well as the interaction parameter in normal direction H_n were fitted to match experimental data obtained from an uniaxial tension test. The material parameters of both fibers and matrix are reported in Table 1. The fiber volume ratio was 0.49.

The influence of the damage interaction parameter in shear H_s was investigated numerically. The resulting major strain distributions for different values of H_s can be seen Fig. 6. Additionally, the corresponding global stress–strain responses for the different H_s-values are depicted in Fig. 7.

As expected, the damage evolution induced by the shear stresses in the matrix leaded to a stronger crack propagation for larger values of H_s. For further investigations concerning the influence of sample size and different loading directions, the reader is referred to [72].

6.2 Damage analysis of textile reinforced composites at the meso-scale

The second example was chosen to illustrate an anisotropic case of damage behavior with interaction of damage variables. In particular, the repeating unit cell (RUC) of a plain weave composite with periodic boundary conditions was considered. The tows were meshed with reduced integration solid elements (C3D8R), whereas for the matrix linear tetrahedral elements were used. In total, the mesh was composed of 30,969 elements.
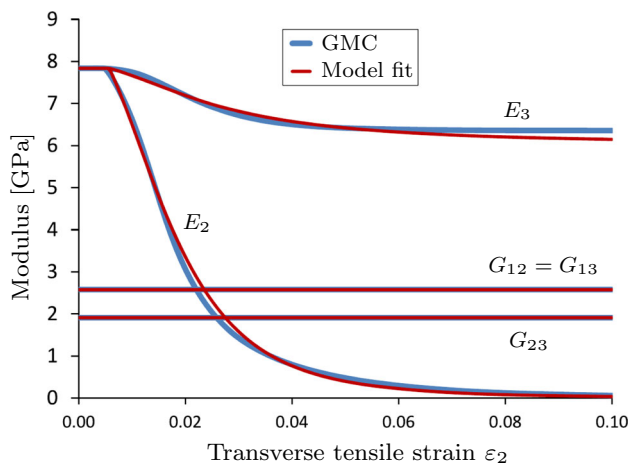
The matrix was epoxy resin modeled by the isotropic damage model without interaction, as given in the previous example (71), where $H_n = 0.75$ and $H_s = 0.55$. The

Table 1 Material parameters of fibers and matrix

	Young's modulus	shear modulus	Poisson's ratio	Hardening/softening parameters			Damage interaction
	(GPa)	(GPa)	(–)	(MPa)	(–)	(MPa)	(–)
Fibers	$E_\parallel = 290$	$G_\parallel = 20$	$\nu_{\parallel\perp} = 0.20$				
	$E_\perp = 20$	$G_\perp = 9$	$\nu_\perp = 0.11$				
Matrix	$E = 3.0$	$G \approx 1.09$	$\nu = 0.38$	$c_1 = 25.7$	$c_2 = -2.8$	$\gamma_0 = 0.45$	$H_n = 0.75$
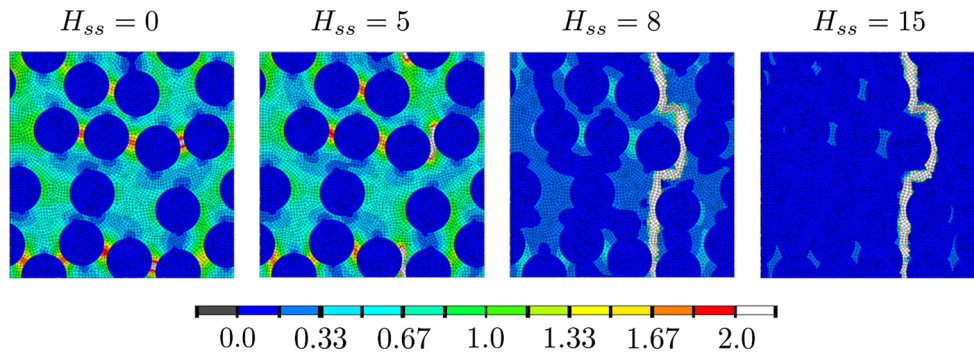
Fig. 6 Major strain distributions in % computed with different values of H_s at an unit cell with 15 fibers subjected to longitudinal shear at an approximate global strain of 1% (scale factor = 5) [72]
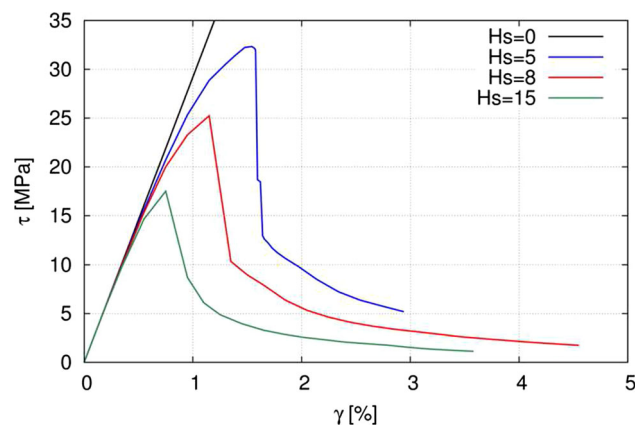
Fig. 7 Global stress–strain responses for different values of H_s at an unit cell with 15 fibers subjected to longitudinal shear [72]

tow consisted of carbon fibers embedded in the same matrix material with a fiber volume fraction of 0.49. The material parameters are the ones presented in Table 1.

First, the tow behavior was predicted numerically by using the Generalized Method of Cells (GMC), which is a semi-analytical micro-scale method (see [3] for details). Then, the

anisotropic damage model was fitted to the results of this GMC-computation. The effective material properties for the tow behavior are given in Table 2.

The resulting damage interaction parameters were

$$
H_{ij} = \begin{bmatrix} 0 & 0 & 0 & 0 & 0 & 0 \\ 0 & 3.1 & 0.77 & 0 & 0 & 0 \\ 0 & 0.77 & 3.1 & 0 & 0 & 0 \\ 0 & 0 & 0 & 1.6 & 0 & 0 \\ 0 & 0 & 0 & 0 & 3.1 & 0 \\ 0 & 0 & 0 & 0 & 0 & 3.1 \end{bmatrix} \tag{72}
$$

Noteworthy, the first row of this matrix was zero, indicating that no damage could occur in the 1-direction, which was the fiber direction in this case. In addition, there was an off-diagonal term which was non-zero, linking the two directions of transverse tension to each other. This link can be demonstrated in Fig. 8, in which the engineering constants are plotted over the applied transverse tensile strain as result of a numerical transverse tensile test.

As can be seen in Fig. 8, the applied loading in 2-direction leaded to a drastic decrease in the Young's modulus E_2 in

Table 2 Material parameters of the tows

	Young's modulus	shear modulus	Poisson's ratio	Hardening/softening parameters		
	(GPa)	(GPa)	(–)	(MPa)	(–)	(MPa)
tow	$E_\parallel = 144$	$G_\parallel = 2.58$	$\nu_{\parallel\perp} = 0.29$	$c_1 = 63$	$c_2 = -4$	$\gamma_0 = 0.45$
	$E_\perp = 7.84$	$G_\perp = 1.91$	$\nu_\perp = 0.39$			

Fig. 8 Evolution of engineering constants of the tow applied to transverse tension loading [11]

loading direction. Additionally, the stiffness E_3 in the other transverse direction is also reduced slightly, while neither the shear moduli nor the stiffness E_1 in fiber direction (not plotted) are effected. This anisotropic damage effect is reflected by the interaction parameter $H_{23} = 0.77$ in (72).
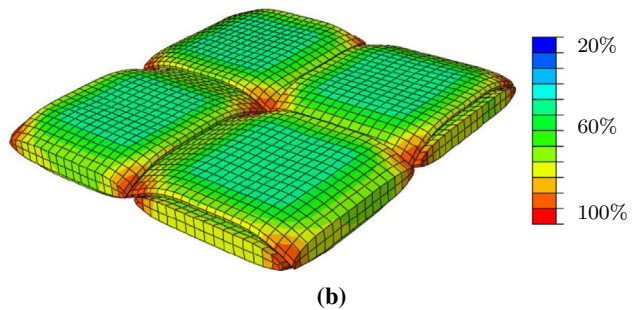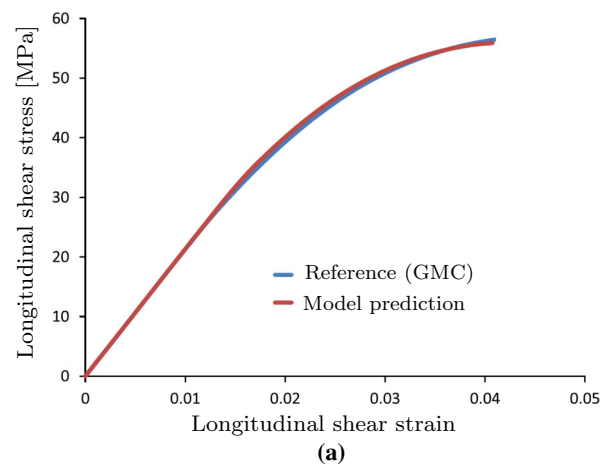
The longitudinal shear response of the plain weave RUC has been investigated. The global stress–strain curve predicted with the proposed model is shown in Fig. 9(a) (red line). For comparison, a reference solution is additionally shown (blue line), which again has been obtained by GMC. Furthermore, local results of the fractional reduction of the effective shear modulus G_{12} are illustrated for the tows in Fig. 9(b) as a measure of the damage in this direction, where 100% defines the undamaged state and e.g. 20% means that the effective shear modulus has been reduced to 20% of its initial (undamaged) value.

For further investigations, particularly with different loading scenarios, the reader is referred to [11].

6.3 Analysis of mode I delamination: double cantilever beam (DCB) Test

In order to evaluate the potential of the proposed damage model for analysis of mode I delamination, the well-known DCB test was considered following the ASTM D5528 standard, see Fig. 10.

The dimensions of the specimen can be found in Table 3. The cantilevers were made from T300/977-2 unidirectional laminates with material parameters provided in Table 4 taken from [42,77]. For the interface layer, material parameters of the neat resign material were chosen, also given in Table 4. Both cantilevers and the interface layer were discretized with eight-node solid elements C3D8R in Abaqus. In total the mesh consisted of 161,348 elements and 210,672 nodes. The loading was applied by prescribing the displacements


Fig. 9 Predicted global and local response of the plain weave RUC under longitudinal shear loading [11]. **a** Global stress–strain response; **b** fractional reduction of effective shear modulus given as ratio of damaged shear modulus over the pristine one (matrix has been removed for illustration)

of the nodes at the top and bottom edges of the cantilevers, respectively. The computations were performed with two different maximum loading step sizes: $\Delta u^+ = 0.1$ mm and $\Delta u^- = 0.01$ mm.

To investigate the influence of the damage hardening/softening function, two different sets of according model parameters were used (see Table 5) defining two different stress–strain relations, see Fig. 11. It should be mentioned, that these parameters were chosen such that they yield different peak stresses of 63 MPa and 70 MPa, respectively, but the same values for the fracture energy.

For comparison, the interface layer was also modeled by finite-thickness continuum-based cohesive elements COH3D8, where two different constitutive relations were applied: a bilinear stress–strain curve and an exponential one, see Fig. 11. For both of these, the peak stress was chosen to be 63 MPa as for the UMAT 1. Noteworthy, the strain value that corresponds to the peak stress value is slightly different for the COH3D8 elements, although in all computations the same elastic material constants were used. The reason for that is the influence of Poisson's ratio, which is accounted for with the fully three-dimensional material model in the
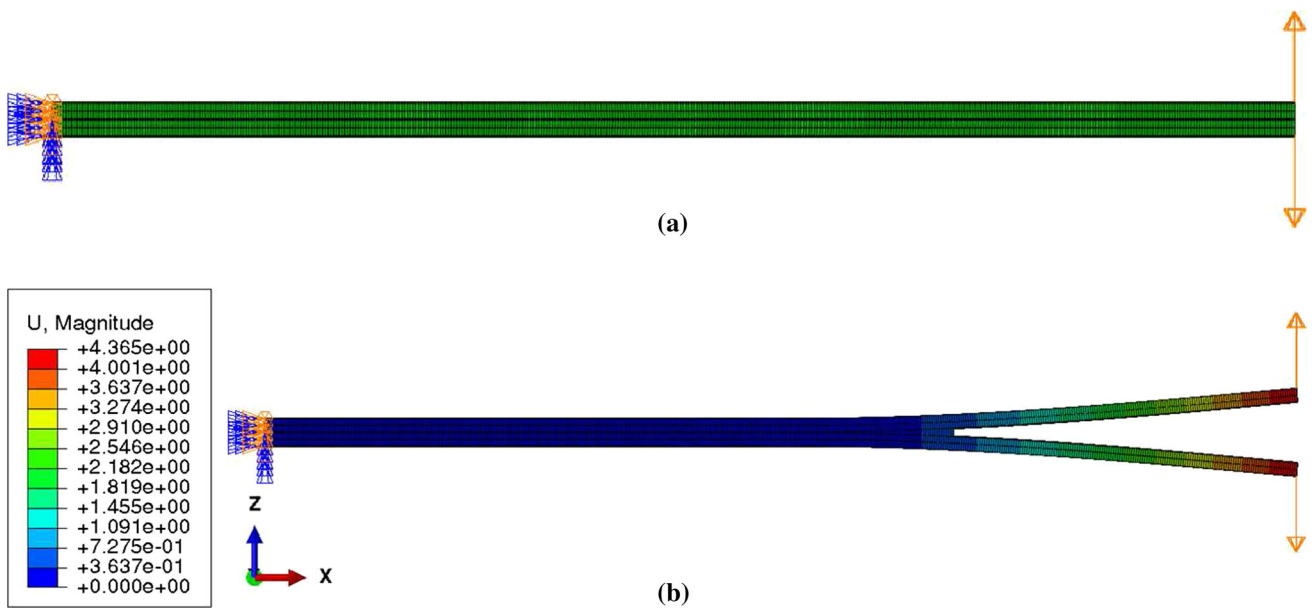
Fig. 10 DCB: System, mesh, boundary conditions, and applied loading. **a** Undeformed configuration; **b** displacement distribution in deformed configuration

Table 3 Dimensions of DCB (mm)

Length	Width	Thickness	Initial crack length	Interface layer thickness
150	25	4	55	0.02

Table 4 Material parameters of cantilevers and interface

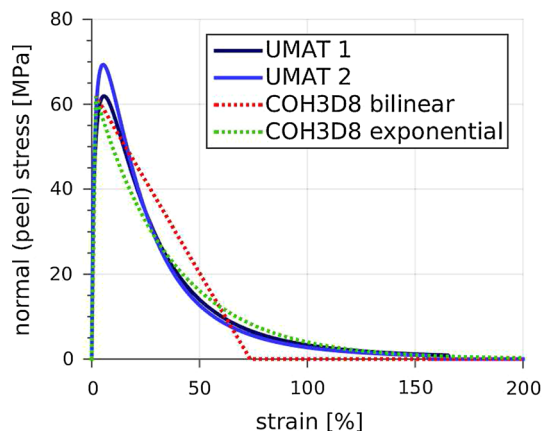|	Young's modulus (GPa)	Shear modulus (GPa)	Poisson's ratio (–)	Fracture energies (J/m^2)	
Cantilever	$E_\parallel = 150$	$G_\parallel = 6$	$\nu_{\parallel\perp} = 0.25$		
	$E_\perp = 11$	$G_\perp = 3.8$	$\nu_\perp = 0.45$		
Interface	$E = 3.2$	$G \approx 1.18$	$\nu = 0.36$	$G_{Ic} = 432$	$G_{IIc} = 945$

Table 5 Damage parameters of interface layer

	Hardening/softening parameters			Damage interaction parameters		
	(MPa)	(–)	(MPa)	(–)	(–)	(–)
UMAT 1	$c_1 = 0.20$	$c_2 = -0.15$	$\gamma_0 = 0.20$	$H_{nn} = 1.0$	$H_{ns} = 1.0$	$H_{ss} = 0.8$
UMAT 2	$c_1 = 0.40$	$c_2 = -0.171$	$\gamma_0 = 0.10$	$H_{nn} = 1.0$	$H_{ns} = 1.0$	$H_{ss} = 1.0$

UMAT but not in the COH3D8. The latter are only able to provide a spring-like one-dimensional response such that lateral contraction is not captured.
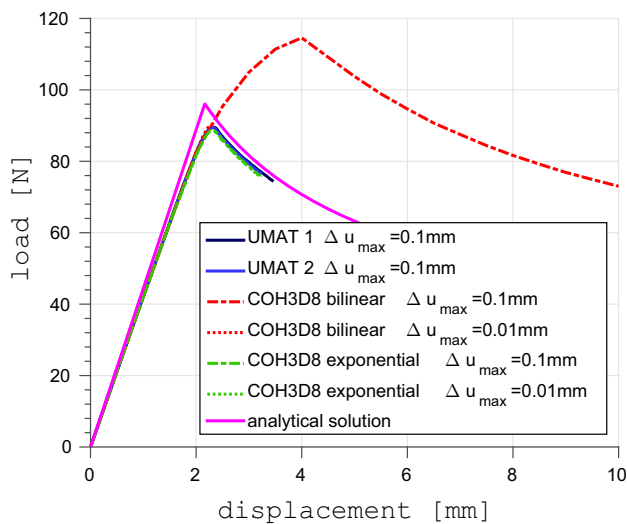
The obtained results for the global load-displacement curve are shown in Fig. 12. As one can see, the two curves for the proposed damage model (solid blue lines) are in agreement with the analytical solution taken from [49] even for the larger maximum loading steps of $\Delta u^+ = 0.1$ mm. Further, the two different sets of parameters used in UMAT 1 and UMAT 2 yield practically the same result showing that the model parameters—including the peak stress value in the stress–strain relation—have only little influence on the global response as long as the fracture energy is preserved.

Additionally, results of the Abaqus elements COH3D8 are also shown in Fig. 12. It was observed, that these were not at all able to reach a converged solution in the post-peak regime for the smaller maximum time steps Δu^- neither for the bilinear nor the exponential constitutive relation (dotted lines in Fig. 12). Even worse, for the bilinear stress–strain constitutive relation, there is a significant difference in peak values and post-peak behavior compared to the reference solution (red dashed line). Only for the exponential case with the larger maximum loading step size Δu^+ (dashed green line)
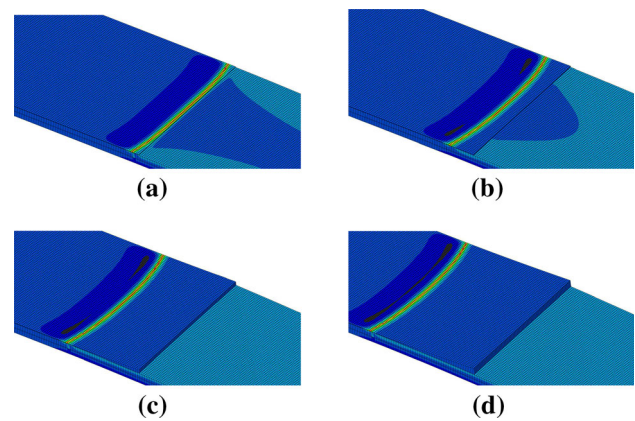
Fig. 11 Stress–strain constitutive response of the proposed damage model (UMAT) and the Abaqus cohesive zone elements COH3D8 with finite thickness

Fig. 12 DCB: comparison of global results between the proposed damage model (UMAT) and the Abaqus cohesive zone elements COH3D8 with finite thickness. The maximum applied loading steps were: $\Delta u^+ = 0.1$ mm and $\Delta u^- = 0.01$ mm
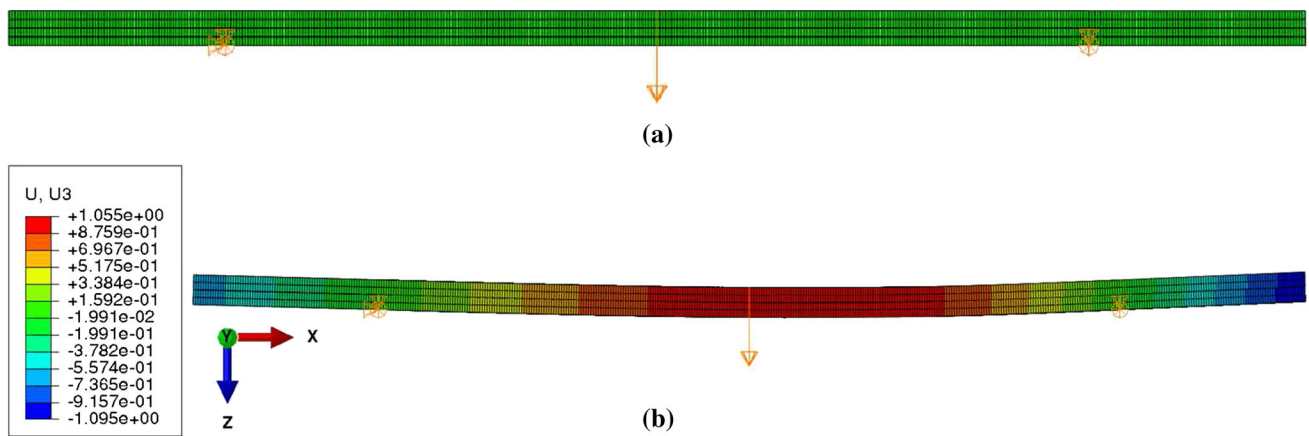

Fig. 13 DCB: predicted normal stress distribution σ_{33} (3-direction: thickness direction). The crack front moved through the interface layer with decreasing loading step from **a** to **d**

Finally, the obtained results for the local normal stress distribution in thickness direction are given in Fig. 13 showing the crack front progressing through the interface layer.

6.4 Analysis of mode II delamination: end notched flexure (ENF) Test

Further, the potential of the proposed damage model for analysis of mode II delamination was investigated by considering the well-known ENF test following the DIN ENF 6034 standard, see Fig. 14. The dimensions of the specimen and the finite element mesh were the same as for the DCB (see Table 3). The distance between the ends of the specimen and the supports was 25 mm, such that the span and the effective initial crack length were 100 mm and 30 mm, respectively. The material parameters were also the same (see Table 4). For the damage model parameters, the ones given in Table 5 for UMAT 1 were applied. As before, the interface layer was additionally modeled by standard Abaqus cohesive elements COH3D8 with finite thickness, where the bilinear and exponential constitutive stress–strain relations were utilized.

The obtained results for the global load-displacement curves are shown in Fig. 15. As one can see, the curves for the proposed damage model (solid blue lines) and the Abaqus cohesive formulation with exponential softening (dashed green lines) were very close to each other. However, the COH3D8 with the bilinear constitutive response (dashed red lines) predicted a higher peak load compared to the other two formulations. Noticeably, all three formulations are more or less in agreement with the analytical solution (magenta solid line) taken from [49,66]. Further, for large displacement values, the result obtained by the proposed UMAT converges asymptotically to the analytical solution using beam theory with two split beams (dashed magenta line), see also [49,66]. Since these results obtained with the larger maximum load-

realistic results could be obtained being close to the analytical solution.

It should be mentioned, that it was not the aim of this paper to improve the performance of the COH3D8 elements. Therefore, stabilizing techniques such as the arc-length method were not adopted, nor were the time stepping control parameters of Abaqus adjusted manually, nor was a mesh refinement conducted, which might have helped to obtain better results, as described e.g. in [71]. Hence, one might be able to solve the given DCB-problem also with the Abaqus elements COH3D8. However, using the same mesh as for the proposed damage model in the UMAT within C3D8R solid elements and applying default values for the control parameters yields unacceptable results.

Fig. 14 ENF: system, mesh, boundary conditions, and applied loading. **a** Undeformed configuration; **b** displacement distribution in deformed configuration
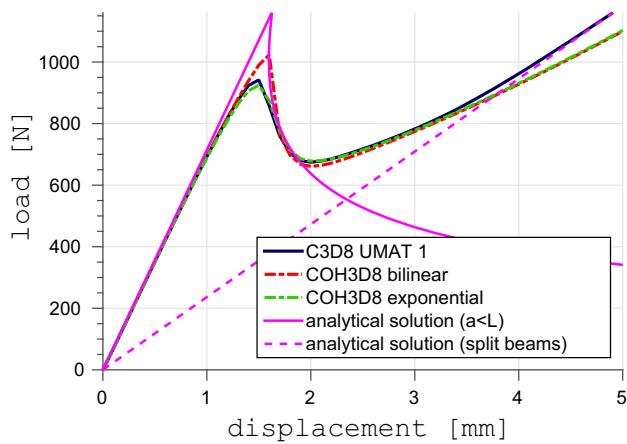
Fig. 15 ENF: comparison of global results between the proposed damage model (UMAT), the Abaqus cohesive zone elements COH3D8 with finite thickness, and the analytical solution
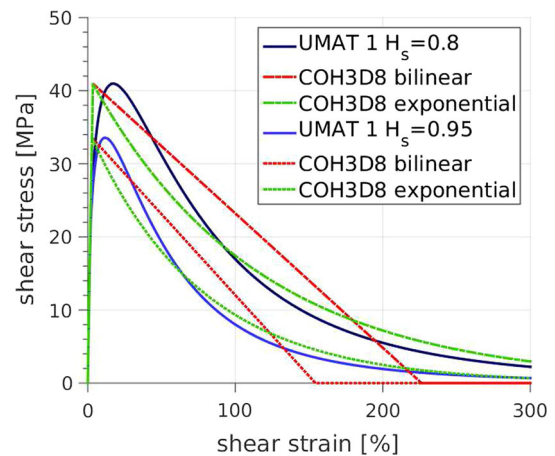
Fig. 16 ENF: stress–strain constitutive responses of the proposed damage model (UMAT) with $H_{ss} = 0.8$ and $H_{ss} = 0.95$, respectively, and the Abaqus cohesive zone elements COH3D8 with finite thickness with $G_{IIc} = 945 \, \text{J/m}^2$ and $G_{IIc} = 514 \, \text{J/m}^2$, respectively

ing step size of $\Delta u^+ = 0.1$ mm were already satisfactory, no smaller time step sizes were investigated.

In order to demonstrate that various ratios of mode-dependent fracture toughness can be accomplished, the shear damage interaction parameter was increased to $H_{ss} = 0.95$ in a second case, which reduced the fracture energy to $G_{IIc} = 514 \, \text{J/m}^2$. The corresponding stress–strain relations are plotted in Fig. 16, whereas the global results are shown in Fig. 17.

Concluding, the obtained results for the local shear stress distribution in longitudinal-thickness direction are given in Fig. 18 showing the crack front progressing through the interface layer.

6.5 Mixed-mode test with proportional loading

Finally, the proposed damaged model was verified for various mixed-mode loading conditions applied to a single element test. As shown in Fig. 19, the lower surface of the considered block was completely fixed, while displacements u_2 and u_3 ($u_1 = 0$) were prescribed on the top surface.

The displacement-controlled proportional loading was given in terms of an angle $\theta \in [0, \pi/4]$, such that

$$u_2 = u^{II} \sin(2\theta) \quad u_3 = u^I \cos(2\theta) \tag{73}$$

where u^I and u^{II} were the displacements at complete failure in pure mode I ($\theta = 0$) and mode II ($\theta = \pi/4$), respectively. For the current investigation, complete failure was defined by a maximum damage variable of 0.99. It is worth to mention, that this limit can be set to any value. If no limit for the damage variables is set, then a tolerance of $tol = 10^{-8}$ is applied such that $d_i \leq 1 - tol$.

The elastic material parameters were the same as for the interface layer in the previous examples (see Table 4).
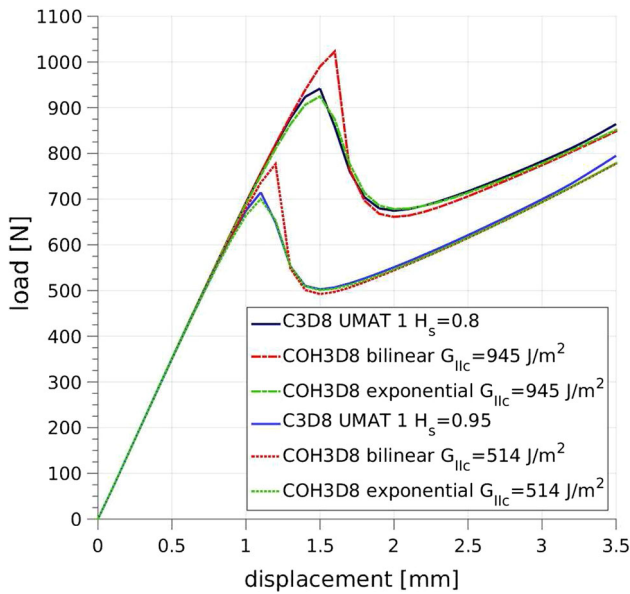
Fig. 17 ENF: comparison of global results between the proposed damage model (UMAT) and the Abaqus cohesive zone elements COH3D8 with finite thickness for two different damage interaction parameters $H_{ss} = 0.8$ ($G_{IIc} = 945$ J/m^2) and $H_{ss} = 0.95$ ($G_{IIc} = 514$ J/m^2)
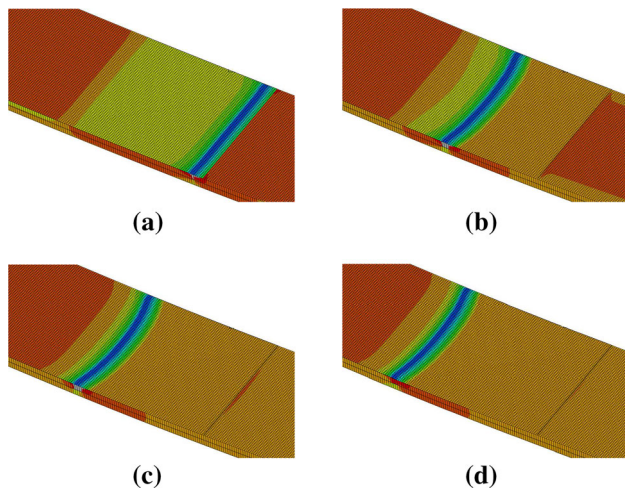

Fig. 18 ENF: predicted shear stress distribution τ_{13} (1-direction: longitudinal direction, 3-direction: thickness direction). The crack front moves through the interface layer with decreasing loading step from **a** to **d**

The hardening/softening parameters were adopted from the UMAT 1 (see Table 5), while the damage interaction parameters were set to $H_{nn} = H_{ns} = H_{ss} = 1.0$.

Seven different values for the angle θ were considered: $\theta = n\,\pi/24$ ($n = 0, 1, \ldots, 6$). For any of these, the resulting dissipated energies G_I and G_{II} were computed and compared to the analytical solution provided by Yuan and Fish [89]:

$$G_I = G_{Ic}\cos^2(2\theta) \qquad G_{II} = G_{IIc}\sin^2(2\theta) \qquad (74)$$
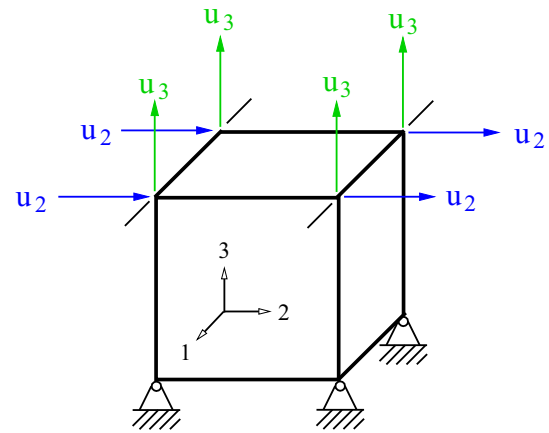
Fig. 19 Mixed-mode loading conditions
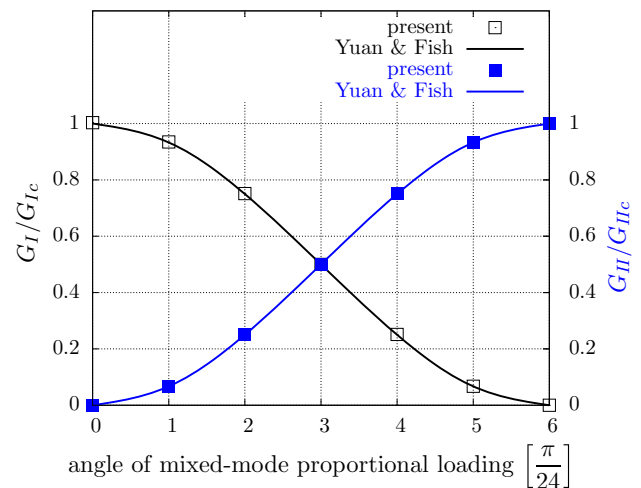
Fig. 20 Dissipated energies scaled with the fracture toughness for various angles of mixed-mode loading in comparison to the analytical solution taken from Yuan and Fish [89]

Results are presented in Fig. 20. As one can see, the simulated results coincide with the analytical ones.

7 Conclusions

A phenomenological progressive damage model has been presented, which is formulated in a thermodynamically consistent manner. The model is able to account for anisotropic damage evolution which is induced by the underlying microstructure of the considered composite. Moreover, the results are mesh independent thanks to the use of a regularization scheme that is based on the fracture energy dissipated during crack opening. Thereby it is guaranteed, that the predicted damage states are reasonable and admissible from physical point of view.

It has been shown that the presented approach can be applied for predicting intralaminar damage propagation as

well as delamination between layers of laminated composite structures. While these different damage modes are typically treated separately, they can be taken into account concurrently by the proposed model. The potential of the approach has been illustrated by five numerical examples: (i) analysis of isotropic damage evolution within the matrix material of a unidirectional fiber reinforced composite sample at the micro-scale; (ii) analysis of the anisotropic damage evolution within the tows of a plain weave composite material at the meso-scale (textile scale); (iii) analysis of delamination induced by tensile loading (mode I) using the DCB test; (iv) analysis of delamination induced by shear loading (mode II) using the ENF test; (v) analysis of the mixed-mode behavior with proportional loading.

Noteworthy, the comparison with analytical solutions as well as Abaqus finite-thickness cohesive elements COH3D8 has shown that the proposed model is well suited for delamination analysis both in mode I and mode II. The obtained results from the DCB as well as ENF test are satisfying. Moreover, in some cases (particularly for the DCB) the Abaqus elements were not able to realistically predict the load-displacement curve for the same mesh which gave accurate results with the proposed damage model. Furthermore, the study of the mixed-mode test has clearly shown that practically any mode mixity—represented by the angle θ—can be accounted for.

Concluding, the proposed model has been shown to be suitable for damage analysis and delamination prediction of laminated composites.

Appendix

Consider the case of only one acting thermodynamic driving force $Y_3 \neq 0$, such that

$$Y_3 = \frac{(\sigma_3)^2}{(1-d_3)^3 E_3} = (1-d_3)E_3\varepsilon_3 \tag{75}$$

Then, according to the evolution equations (44), the rates of the corresponding damage variable $\dot{d}_3$ and the hardening/softening variable $\dot{\delta}$ read

$$\dot{d}_3 = \sqrt{H_{33}}\dot{\lambda} \qquad \dot{\delta} = -\dot{\lambda} \tag{76}$$

Hence, choosing $H_{33} = 1$, one gets $\dot{\delta} = -\dot{d}_3$. Since $\delta(0) = 0$ as well as $d_3(0) = 0$, this also implies $\delta = -d_3$. In this case,

the damage surface is given by

$$f = Y_3 - c_1\left(e^{-d_3/c_2} - 1\right) - \gamma_0 = 0 \tag{77}$$

Substituting Y_3 from (75) yields

$$f = (1-d_3)E_3\varepsilon_3 - c_1\left(e^{-d_3/c_2} - 1\right) - \gamma_0 = 0 \tag{78}$$

If two points $(\sigma_3^I, \varepsilon_3^I)$ and $(\sigma_3^{II}, \varepsilon_3^{II})$ are given, the corresponding damage variables can be computed as follows:

$$d_3^I = 1 - \sqrt{\frac{\sigma_3^I}{E_3\varepsilon_3^I}} \qquad d_3^{II} = 1 - \sqrt{\frac{\sigma_3^{II}}{E_3\varepsilon_3^{II}}} \tag{79}$$

Evaluating the damage surface (78) at point $(\sigma_3^I, \varepsilon_3^I)$ yields the following equation:

$$(1-d_3^I)E_3\varepsilon_3^I - c_1\left(e^{-d_3^I/c_2} - 1\right) - \gamma_0 = 0 \tag{80}$$

which can be rewritten as

$$a_1 - c_1\left(e^{-d_3^I/c_2} - 1\right) = 0 \tag{81}$$

where the following abbreviation has been introduced:

$$a_1 = (1-d_3^I)E_3(\varepsilon_3^I)^2 - \gamma_0 \tag{82}$$

From (81), the relation between c_1 and c_2 is obtained as

$$c_1 = \frac{a_1}{(e^{-d_3^I/c_2} - 1)} \tag{83}$$

Finally, this relation is inserted into the damage surface, which is evaluated at the second point $(\sigma_3^{II}, \varepsilon_3^{II})$, leading to

$$a_2 - \frac{a_1}{(e^{-d_3^I/c_2} - 1)}\left(e^{-d_3^{II}/c_2} - 1\right) = 0 \tag{84}$$

$$\text{where:} \quad a_2 = (1-d_3^{II})E_3(\varepsilon_3^{II})^2 - \gamma_0 \tag{85}$$

which can be expressed as

$$a_2\left(e^{-d_3^I/c_2} - 1\right) - a_1\left(e^{-d_3^{II}/c_2} - 1\right) = 0 \tag{86}$$

References

1. Abaqus finite element software. Dassault Systemes Simulia Corp. 2014
2. Aboudi J (2011) The effect of anisotropic damage evolution on the behavior of ductile and brittle matrix composites. Int J Solids Struct 48:2102–2119

3. Aboudi J, Arnold SM, Bednarcyk B (2013) Micromechanics of composite materials—a generalized multiscale approach, 1st edn. Elsevier, New York

4. Balzani C, Wagner W (2008) An interface element for the simulation of delamination in unidirectional fiber-reinforced composite laminates. Eng Fract Mech 75:2597–2615

5. Barbero EJ (2008) Finite element analysis of composite materials, 1st edn. CRC Press, Boca Raton

6. Barbero EJ (2013) Finite element analysis of composite materials, 2nd edn. CRC Press, Boca Raton

7. Bažant ZP, Oh BH (1983) Crack band theory for fracture of concrete. Matériaux et Constructions 16:155–177

8. Bažant ZP, Pijaudier-Cabot G (1989) Measurement of characteristic length of nonlocal continuum. J Eng Mech 115:755–767

9. Bažant ZP, Planas J (1998) Fracture and size effect in concrete and other quasibrittle materials. CRC Press, Boca Raton

10. Bednarcyk BA, Aboudi J, Arnold SM (2010) Micromechanics modeling of composites subjected to multiaxial progressive damage in the constituents. AIAA J 48:1367–1378

11. Bednarcyk BA, Stier B, Simon JW, Reese S, Pineda EJ (2015) Meso- and micro-scale modeling of damage in plain weave composites. Compos Struct 121:258–270

12. Betten J (2001) Mathematical modelling of materials behaviour under creep conditions. Appl Mech Rev 54:107–132

13. Betten J (2005) Creep mechanics, 2nd edn. Springer, Berlin

14. Borkowski L, Chattopadhyay A (2015) Multiscale model of woven ceramic matrix composites considering manufacturing induced damage. Compos Struct 126:62–71

15. Camanho PP, Matthews FL (1999) Delamination onset prediction in mechanically fastened joints. J Compos Mater 33:906–927

16. Chaboche J (1988) Continuum damage mechanics—part I: general concepts, part II: damage growth, crack initiation, and crack growth. J Appl Mech 55:59–71

17. Chow CL, Wang J (1987) An anisotropic theory of continuum damage mechanics for ductile fracture. Eng Fract Mech 21:547–558

18. de Borst R, Remmers JJC (2006) Computational modeling of delamination. Compos Sci Technol 66:713–722

19. Desmorat R, Gatuingt F, Ragueneau F (2007) Nonlocal anisotropic damage model and related computational aspects for quasi-brittle materials. Eng Fract Mech 74:1539–1560

20. Dimitri R, Trullo M, de Lorenzis L, Zavarise G (2015) Coupled cohesive zone models for mixed-mode fracture: a comparative study. Eng Fract Mech 148:145–179

21. Duddu R, Waisman H (2013) A nonlocal continuum damage mechanics approach to simulation of creep fracture in ice sheets. Comput Mech 51:961–974

22. Falzon BG, Apruzzese P (2011) Numerical analysis of intralaminar failure mechanisms in composite structures—part II: applications. Compos Struct 93:1047–1053

23. Fish J, Jiang T, Yuan Z (2012) A staggered nonlocal multiscale model for a heterogeneous medium. Int J Numer Methods Eng 91:142–157

24. Gupta AK, Patel BP, Nath Y (2013) Continuum damage modeling of composite laminated plates using higher order theory. Compos Struct 99:141–151

25. Hansen NR, Schreyer HL (1994) A thermodynamically consistent framework for theories of elastoplasticity coupled with damage. Int J Solids Struct 31:359–389

26. Hashin IZ, Rotem A (1973) A fatigue failure criterion for fiber reinforced materials. J Compos Mater 7:448–464

27. Hoover C, Bažant ZP (2014) Cohesive crack, size effect, crack band and work-of-fracture models compared to comprehensive concrete fracture tests. Int J Fract 187:133–143

28. Jirasek M, Bauer M (2012) Numerical aspects of the crack band approach. Comput Struct 110–111:60–78

29. Kachanov LM (1986) Introduction to continuum damage mechanics. Nijhoff Publishers, Dordrecht

30. Kanoute P, Boso DP, Chaboche JL, Schrefler BA (2009) Multiscale methods for composites: a review. Arch Comput Methods Eng 16:31–75

31. Kenik D, Nelson E, Robbins D, Mabson G (2012) Developing guidelines for the application of coupled fracture/continuum mechanics-based composite damage models for reducing mesh sensitivity. AIAA J 1618:1–19

32. Klusemann B, Svendsen B (2012) Homogenization modeling of thin-layer-type microstructure. Int J Solids Struct 49:1828–18389

33. Klinge S, Hackl K (2012) Application of the multiscale FEM to the modeling of nonlinear composites with a random microstructure. Int J Multiscale Comput Eng 10:213–227

34. Krajcinovic D (1998) Selection of damage parameter—art or science? Mech Mater 28:165–179

35. Krajcinovic D, Basista M, Sumarac D (1991) Micromechanically inspired phenomenological damage model. J Appl Mech 58:305–310

36. Kroll U, Matzenmiller A (2015) Parameter identification of a damage model for the lifetime prediction of adhesively bonded joints. Appl Mech Mater 784:300–307

37. Kuhl E, Ramm E, de Borst R (2000) An anisotropic gradient damage model for quasi-brittle materials. Comput Methods Appl Mech Eng 183:87–103

38. Le JL, Elias J (2016) A Probabilistic Crack Band Model for Quasibrittle Fracture. J Appl Mech 83(051005):1–7

39. Lemaitre J (1985) Mathematical modelling of materials behaviour under creep conditions. Appl Mech Rev 54:107–132

40. Lemaitre J (1996) A course on damage mechanics, 2nd edn. Springer, Berlin

41. Lemaitre J, Chaboche J (1990) Mechanics of solid materials. Cambridge University Press, Cambridge

42. Li B, Li Y, Su J (2014) A combined interface element to simulate interfacial fracture of laminated shell structures. Composites B 58:217–227

43. Lin SP, Chen JS, Liang S (2016) A damage analysis for brittle materials using stochastic micro-structural information. Comput Mech 57:371–385

44. Liu Y, Filonova V, Hu N, Fish J, Yuan Z, Belytschko T (2014) A regularized phenomenological multiscale damage model. Int J Numer Methods Eng 99:867–887

45. McAuliffe C, Waisman H (2013) Mesh insensitive formulation for initiation and growth of shear bands using mixed finite elements. Comput Mech 51:807–823

46. Matzenmiller A, Lubliner J, Taylor RL (1995) A constitutive model for anisotropic damage in fiber-composites. Mech Mater 20:125–152

47. Melro AR, Camanho PP, Pires FMA, Pinho ST (2013) Micromechanical analysis of polymer composites reinforced by unidirectional fibres: part I constitutive modelling. Int J Solids Struct 50:1897–1905

48. Meyer P, Waas AM (2016) FEM predictions of damage in continous fiber ceramic matrix composites under transverse tension using the crack band method. Acta Mater 102:292–303

49. Mi Y, Chrisfield MA, Davies GAO, Hellweg HB (1998) Progressive delamination using interface elements. J Compos Mater 32:1246–1272

50. Maimi P, Camanho PP, Mayugo JA, Davila CG (2007) A continuum damage model for composite laminates: part I constitutive model. Mech Mater 39:897–908

51. Maimi P, Mayugo JA, Camanho PP (2008) A Three-dimensional Damage Model for Transversely Isotropic Composite Laminates. J Compos Mater 42:2717–2745

52. Needleman A (1988) Material rate dependence and mesh sensitivity in localization problems. Comput Methods Appl Mech Eng 67:69–85

53. Nguyen GD, Nguyen CT, Nguyen VP, Bui HH, Shen L (2016) A size-dependent constitutive modelling framework for localised failure analysis. Comput Mech 58:257–280

54. Niazi MS, Wisselink HH, Meinders T (2013) Viscoplastic regularization of local damage models: revisited. Comput Mech 51:203–216

55. Oliver J (1989) A consistent characteristic length for smeared cracking models. Int J Numer Methods Eng 28:461–474

56. Peerlings RHJ, de Borst R, Brekelmans WAM, de Vree JHP (1996) Gradient enhanced damage for quasi-brittle materials. Int J Numer Methods Eng 39:3391–3403

57. Pela L, Cervera M, Roca P (2013) An orthotropic damage model for the analysis of masonry structures. Constr Build Mater 41:957–967

58. Pela L, Cervera M, Oller S, Chiumenti M (2014) A localized mapped damage model for orthotropic materials. Eng Fract Mech 124–125:196–216

59. Pena E (2011) A rate dependent directional damage model for fibred materials: application to soft biological tissues. Comput Mech 48:407–420

60. Petracca M, Pela L, Rossi R, Oller S, Camata G, Spacone E (2016) Regularization of first order computational homogenization for multiscale analysis of masonry structures. Comput Mech 57:257–276

61. Pineda EJ, Waas AM (2013) Numerical implementation of a multiple-ISV thermodynamically-based work potential theory for modeling progressive damage and failure in fiber reinforced laminates. Int J Fract 182:93–122

62. Rah K, van Paepegem W, Degriek J (2013) An optimal versatile partial hybrid stress solidshell element for the analysis of multilayer composites. Int J Numer Methods Eng 93:201–223

63. Richard B, Ragueneau F (2013) Continuum damage mechanics based model for quasi brittle materials subjected to cyclic loadings: formulation, numerical implementation and applications. Eng Fract Mech 98:383–406

64. Shojaei A, Li G, Fish J, Tan PJ (2014) Multi-scale constitutive modeling of ceramic matrix composites by continuum damage mechanics. Int J Solids Struct 51:4068–4081

65. Sidoroff F (1981) Description of anisotropic damage application to elasticity. Physical nonlinearities in structural analysis. Springer, Berlin, pp 237–244

66. Silva MAL, de Moura MFSF, Morais JJL (2006) Numerical analysis of the ENF test for mode II wood fracture. Compos Part A 37:1334–1344

67. Simon JW, Höwer D, Stier B, Reese S (2015) Meso-mechanically motivated modeling of layered fiber reinforced composites accounting for delamination. Compos Struct 122:477–487

68. Simon JW, Stier B, Reese S (2015) Numerical analysis of layered fiber composites accounting for the onset of delamination. Adv Eng Softw 80:4–11

69. Slobbe AT, Hendriks MAN, Rots JG (2013) Systematic assessment of directional mesh bias with periodic boundary conditions: applied to the crack band model. Eng Fract Mech 109:186–208

70. Sluys LJ, de Borst R (1992) Wave propagation and localization in a rate-dependent cracked medium—model formulation and one-dimensional examples. Int J Solids Struct 29:2945–2958

71. Song K, Davila CG, Rose CA (2008) Guidelines and parameter selection for the simulation of progressive delamination. (2008) ABAQUS User's Conference. Newport, RI, United States

72. Stier B, Bednarcyk BA, Simon JW, Reese S (2015) Investigation of micro-scale architectural effects on damage of composites. *NASA/TM2015-218740*

73. Stier B, Simon JW, Reese S (2015) Finite element analysis of layered fiber composite structures accounting for the materials microstructure and delamination. Appl Compos Mater 22:171–187

74. Tavares RP, Melro AR, Bessa MA, Turon A, Liu WK, Camanho PP (2016) Mechanics of hybrid polymer composites: analytical and computational study. Comput Mech 57:405–421

75. Toro S, Sanchez PJ, Podesta JM, Blanco PJ, Huespe AE, Feijoo RA (2016) Cohesive surface model for fracture based on a two-scale formulation: computational implementation aspects. Comput Mech 58:549–585

76. Turon A, Camanho PP, Costa J, Davila CG (2006) A damage model for the simulation of delamination in advanced composites under variable-mode loading. Mech Mater 38:1072–1089

77. Turon A, Davila CG, Camanho PP, Costa J (2007) An engineering solution for mesh size effects in the simulation of delamination using cohesive zone models. Eng Fract Mech 74:1665–1682

78. Voyiadjis GZ, Deliktas B (2000) A coupled anisotropic damage model for the inelastic response of composite materials. Comput Methods Appl Mech Eng 183:159–199

79. Voyiadjis GZ, Shojaei A, Li G (2011) A thermodynamic consistent damage and healing modelhealing materials. Int J Plast 27:1025–1044

80. Waffenschmidt T, Polindara C, Menzel A, Blanco S (2014) A gradient-enhanced large-deformation continuum damage model for fibre-reinforced materials. Comput Methods Appl Mech Eng 268:801–842

81. Williams KV, Vziri R, Poursartip A (2003) A physically based continuum damage mechanics model for thin laminated composite structures. Int J Solids Struct 40:2267–2300

82. Wang WM, Sluys LJ, de Borst R (1997) Viscoplasticity for instabilities due to strain softening and strain-rate softening. Int J Numer Methods Eng 40:3839–3864

83. Whang C, Zhang H, Shi G (2012) 3D Finite element simulation of impact damage of laminated plates using solid-shell interface elements. Appl Mech Mater 130–134:766–770

84. Wu JY, Li J, Faria R (2006) An energy release rate-based plastic-damage model for concrete. Int J Solids Struct 43:583–612

85. Wu L, Sket F, Molina-Aldareguia JM, Makradi A, Adam L, Doghri I, Noels L (2015) A study of composite laminates failure using an anisotropic gradient-enhanced damage mean-field homogenization model. Compos Struct 126:246–264

86. Xie D, Waas AM (2006) Discrete cohesive yone model for mixed-mode fracture using finite element analysis. Eng Fract Mech 73:1783–1796

87. Xin SH, Wen HM (2015) A progressive damage model for fiber reinforced plastic composites subjected to impact loading. Int J Impact Eng 75:40–52

88. Xu W, Waas AM (2016) Modeling damage growth using the crack band model; effect of different strain measures. Eng Fract Mech 152:126–138

89. Yuan Z, Fish J (2016) Are the cohesive zone models necessary for delamination analysis? Comput Methods Appl Mech Eng 310:567–604

90. Ye L (1988) Role of matrix resin in delamination onset and growth in composite laminates. Compos Sci Technol 33:257–277

91. Zheng Q-S, Betten J (1996) On damage effective stress and equivalence hypothesis. Int J Damage Mech 5:219–240

92. Zienkiewicz OC, Taylor RL (2005) The finite element method for solid and structural mechanics, 6th edn. Elsevier, Amsterdam